On the formation of thrust fault-related landforms in Mercury's Northern Smooth Plains: A new mechanical model of the lithosphere

Jingchun Xie[1,2], **Chengli Huang**[3,2,4] **and Mian Zhang**[3,4]

[1]Shanghai Astronomical Observatory, Chinese Academy of Sciences, Shanghai 200030, China
[2]School of Physical Science and Technology, ShanghaiTech University, Shanghai 201210, China
[3]CAS Key Laboratory of Planetary Sciences, Shanghai Astronomical Observatory, Chinese Academy of Sciences, Shanghai 200030, China
[4]School of Astronomy and Space Science, University of Chinese Academy of Sciences, Beijing 100049, China

Key Points:

- A new mechanical model allowing for the weak layer in the lithosphere deduced by thin-rooted deformation is proposed
- A 2-D numerical simulation is conducted, from which a consistent surface topography with observed thrust fault-related landforms is obtained
- This model refines the mechanical structure of Mercury's lithosphere, worthy of further application

Corresponding author: Chengli Huang, clhuang@shao.ac.cn

Abstract

There are a large number of tectonic shortening structures distributed across the planet Mercury, which are interpreted as the product of lithospheric deformation mainly attribute to secular cooling of the planetary interior. As the largest single volcanic deposit on Mercury, the northern smooth plains (NSP) is dominated by thrust fault-related landforms, showing particularity in their geomorphic features and requires an assumed weak layer at a shallow depth to account for the thin-rooted deformation in the lithosphere. However, there is a lack of proper mechanical model to account for such layer in the lithosphere beneath the NSP. In this work, we propose a new mechanical model allowing for a mechanically discontinuous lithosphere by introducing the semi-brittle deformation style, with detailed model configurations. Our work simulates a compressive dynamic process to mimic the formation for thrust fault-related landforms in the NSP of 3.8 billion years ago through 2-D numerical simulations. This simulation lasts for 70 million years, resulting in a concentrated and high strain rate region (i.e., weak layer) at shallow depth in the crust and geomorphically consistent surface topography with commonly observed thrust fault-related landforms. Geomorphically steady surface relief suggests that these shortening landforms were formed in a short period of time on geological time scales, and have maintained their basic geomorphic features to present day. The potential influence of the topography at the crust-mantle boundary on the surface relief is also recognized. Additional set of numerical simulations emphasizes that a larger topography facilitates the formation for higher surface relief.

Plain Language Summary

One of the most striking features of Mercury's surface is the global distributed shortening geological landforms. The formation and geomorphic characteristics of these tectonic features are associated with the mechanical structure of lithosphere. For the single largest volcanically resurfaced smooth terrain termed the northern smooth plains on Mercury, there is neither satisfied lithospheric mechanical model nor numerical simulations allowing for a mechanically discontinuous lithosphere. In this paper, we propose a new lithospheric mechanical model to mimic a formation process of thrust fault-related landforms of 3.8 billion years ago through 2-D numerical simulation. Our work is tested with an open-source finite element mantle convection code, resulting in an equivalent weak layer and geomorphically consistent surface relief with the observed thrust fault-related landforms. Additional numerical simulations are implemented to investigate the influence of the topography at the crust mantle boundary on the surface relief, our results suggest that a larger interface topography facilitates the formation for a higher surface relief. The obtained surface reliefs indicate that these shortening landforms were formed in a short period time and have maintained their basic geomorphic features to present time.

1 Introduction

Previous studies have shown that there are numerous geometries of shortening tectonic features distributed across the planet Mercury (e.g., Watters et al., 2009; Solomon et al., 2018). These geological structures are interpreted as one of the products of the shrinkage and failure of the lithosphere, which is mainly attributed to the stress driven by the secular cooling of the planetary interior (Byrne et al., 2014, 2018; Banks et al., 2015; Klimczak et al., 2019). Geomorphic works suggest that the most representative geological landforms are lobate scarps, wrinkle ridges and high-relief ridges, which are the surface manifestation of the thrust fault, deforming almost all major geological units on Mercury (e.g., Watters et al., 2009; Banks et al., 2015; Klimczak et al., 2019; Watters et al., 2021). Global maps imaged by NASA's MESSENGER mission reveal that about 27% of the Mercury's surface is covered by extensive smooth plains, with the largest single volcanic deposit termed the northern smooth plains (NSP) (Head et al., 2011; Denevi et al., 2013; Ostrach et al., 2015; Du et al., 2020). The NSP is a volcanically resurfaced smooth terrain buried by hundreds to thousands of meters of volcanic deposits (Ostrach et al., 2015), newly estimated thickness of the crust underlying the NSP constrain its value to an average of 19 km by analyzing the relationship between the crustal thickness and mantle melting production (Beuthe et al., 2020). Viewed from the surface, the NSP is abundant in ghost craters and thrust fault-related landforms, where the dominated shortening features are wrinkle ridges and lobate scarps (Byrne et al., 2014). Compared to their counterparts in other geological terrains in Mercury, these landforms show less relief and shorter length (Byrne et al., 2014; Solomon et al., 2018; Crane & Klimczak, 2019; Peterson et al., 2019). Interpretation of the visible geomorphic characteristics on the surface provides an opportunity to explore the subsurface architecture and the behind dynamical mechanisms, which can offer important information about the evolutionary history of Mercury (e.g., Peterson et al., 2020; Watters, 2021).

The principle of initiation of thrust fault requires that the stress imposed by the environment exceeds the limit that the lithosphere can withstand, with the latter being controlled by a variety of factors including the ambient temperature, strain rate and rock's composition and so on (Karato & Wu, 1993; D. Kohlstedt et al., 1995; D. L. Kohlstedt & Mackwell, 2009; Klimczak, 2015; Katayama, 2021). Theoretical calculations rely on the lithospheric strength model, in which the most common and classic strength model known as elastic dislocation model has been applied to recur the subsurface mechanical structure beneath Mercury's intercrater plains (ICP), via the interpretation of the surface shortening landforms (e.g., Watters et al., 2002; Nimmo & Watters, 2004; Egea-González et al., 2012). Applications of elastic dislocation model collectively imply that the fault roots at deep depths, forming lithospheric-scale fault, as a result from the deformation in a mechanically homogenous lithosphere under substantial horizontal compressive stress (Solomon et al., 2018). However, in recent years, detailed tectonic maps drawn by several authors reveal the trends in how thrust fault-related landforms oriented and organized in the NSP, and classify the main deformation style of the lithosphere as thin-rooted by comparsion with Earth analogues and patterns acquired by physical models, collectively suggest a weal layer (or décollement) at shallow depth beneath the NSP to account for the observed geomorphic characteristics under low strain rate (Byrne et al., 2014; Watters et al., 2015; Crane & Klimczak, 2019; Peterson et al., 2019, 2020; Watters et al., 2021). So far, neither the thickness nor the constituent that makes up the weak layer has been well constrained, whereas the only consensus is the possible scenario of the formation for such layer, that is, the burial of impact-induced megaregolith layer by subsequent multi-sequence volcanic eruptions, where faults root and propagate upward (Byrne et al., 2014; Watters et al., 2015). More importantly, the implication deduced from the idea of the presence of weak layer is a mechanically discontinuous crust or lithosphere, which is contradictory to the conclusion suggested by elastic dislocation model used in prior works. Therefore, an appropriate strength model allowing for a mechanically discontinuous lithosphere is still an open issue, in which constantly updated knowledge of Mercury should also be taken into account.

In this paper, we propose a new strength model allowing for a mechanically discontinuous lithosphere beneath the northern smooth plains of Mercury, as a result of a comprehensively considered with ambient temperature, strain rate and rheology and other factors. By implementation of 2-D numerical simulation through an open-source finite-element mantle convection code - Advanced Solver for Problems in Earth's ConvecTion, ASPECT (Kronbichler et al., 2012; Heister et al., 2017), we obtain a concentrated and high strain rate region equivalent to the weak layer within the crust at shallow depth and well consistent surface topography of thrust fault-related landforms discovered in the NSP. This work is structured as follows. First, we introduce the physical model in section 2, followed by the discussion on model configuration in section 3. Lastly, we present our results, discussion and conclusion in turn.

2 Physical Model

For the 2-D numerical simulation, we first apply an incompressible, linear Maxwell model to take visco-elasticity of the mantle into account. The constitutive equation for all materials is (e.g., Moresi et al., 2003):

$$\frac{\tau}{2\eta} + \frac{\bar{\tau}}{2\mu} = \hat{D}_v + \hat{D}_e = \hat{D} \tag{1}$$

Where τ is the deviatoric stress tensor, μ is the elastic shear modulus, η is the shear viscosity, and $\bar{\tau}$ is the Jaumann corotational stress rate tensor. $\hat{D_v}$ and $\hat{D_e}$ are the viscous part and elastic component of the deviatoric strain rate tensor, respectively. A full discussion on this equation can be found in, e.g., Moresi et al. (2003).

Incorporating the elastic force term, the basic equations set describing the conservation of mass, momentum and energy is given by (Moresi et al., 2003):

$$\nabla \cdot u = 0 \tag{2}$$

$$\tau_{ij,j}^{t+\Delta t^e} - \nabla P + f_i + F_i^{e,t} = 0 \tag{3}$$

$$\rho c \frac{\partial T}{\partial t} = \frac{\partial}{\partial x_i}(k \frac{\partial T}{\partial x_i}) + H_R + H_D \tag{4}$$

Where u is the velocity, P is the pressure, and f_i is the specific body force, $F_i^{e,t}$ is the elastic force term. In Eq.(4), ρ is the density, c is the specific heat capacity, and the last three terms on the right side represent the conductive heat, radiogenic heat and viscous dissipation, respectively.

The radiogenic heat term in W/m^3 has the following form (e.g., Michel et al., 2013):

$$H_R(x,t) = \rho_x \sum_i Q_i^0 0.5^{t/\mu_i} \tag{5}$$

Where ρ is the average density, x is the index used to indicate different geological layers (e.g., the crust). Q^0 is the initial radiogenic heating rate in W/kg, i is the index denoting radiogenic heating elements (RHEs), including the element potassium (K), thorium (Th) and uranium (U) (Peplowski et al., 2011). μ and t are half-decay time and time, respectively.

For the viscous dissipation, it is given by (e.g., Thielmann & Kaus, 2012):

$$H_D = \zeta \tau : \dot{\epsilon}^v \tag{6}$$

Where ζ is the heat conversion efficiency, it depends on whether other deformational mechanisms are taken into account. In this work, ζ is set to 1, meaning that we assume that all dissipation energy is converted into heat (e.g., Schmalholz et al., 2018). τ is the deviatoric stress tensor and $\dot{\epsilon}^v$ is the visco-plastic component of the deviatoric strain rate tensor.

3 Model Configuration

The implementation of numerical simulation via ASPECT requires specific configuration of the model when initializing. This step is necessary, because the initial state of any numerical simulations has great impact on the final results. In this section, we primarily concentrate on key configurations, including the initial conditions (initial temperature profile plus the background bulk strain rate), rheology and lithology of the research domain.

3.1 Initial Conditions

The discussions on the initial conditions focus on the initial temperature profile and the applied background bulk strain rate of the research domain. We first assume that the research domain only covers the crust and the lithosphere-mantle rather than the whole outer silicate shell of Mercury. The main reasons are two-fold. Firstly, the average penetration depth of most thrust faults in the NSP is shallow (e.g., Crane & Klimczak, 2019), a full-scale geometry (i.e., a silicate shell with thickness of around 400 km) may affect the display of result. Secondly, the solution to the profile of temperature is easier to solve in the lithosphere.

In order to obtain a representative initial temperature profile, following our previous work (Xie et al., 2022), we carry out a 1-D parametric global evolution model of Mercury (refer to Appendix A). The 1-D model radially divides the planet into several layers (e.g., the crust, thermal boundaries, convecting mantle), with the descriptions of energy-related equations of each layer. The model will iterate until self-consistent results are obtained, providing an outline of the evolutionary picture of Mercury. One additional advantage of this model is the flexibility to specify the truncation time of the model runs. Studies on the timing of the shortening tectonic features suggest that most thrust faulting underway at 3.8±0.2 Ga before present (b.p) (e.g., Giacomini et al., 2015, 2020; Crane & Klimczak, 2017), which is the time of our interest. Therefore, the results given below are all at 3.8 Ga b.p.

After the 1-D parametric model running done (Fig A2), we have crust and lithosphere-mantle with the thickness of around 19.1 km and 110.8 km, respectively. The first result is close to the value of the crustal thickness beneath the NSP of 19±3 km (Beuthe et al., 2020). Correspondingly, the radiogenic heating production rate (RHPR) are about 9.37×10^{-11} W/kg and 9.37×10^{-12} W/kg at 3.8 Ga b.p. The value of the crustal RHPR is in line with the result calculated by the Gamma-Ray Spectrometer measured data (Peplowski et al., 2011). In the end, the initial temperature profile over time derived from Eq.(A1-2) is shown in Fig 2, where the temperature at the crust-mantle boundary (T_{CrMB}) and the bottom of the lithosphere-mantle (T_l) are about 754 K and 1435 K at the time of 3.8 Ga b.p.

The second point is about the background bulk strain rate (hereinafter referred to as strain rate). For Mercury, favored values adopted by strength models are of the order of 10^{-17} s^{-1} (e.g., Zuber et al., 2010; Egea-González et al., 2012). However, recent study on the stratigraphic relationships of thrust fault-related landforms with craters limited the strain rate at the onset of faulting to the order of $10^{-20}\sim10^{-21}$ s^{-1} (Crane & Klimczak, 2017). Moreover, if the elastic properties of the rock are taken into account, the strain rate during the lithospheric elastic deformation processes is probably between the order of 10^{-19} and 10^{-20} s^{-1}(Klimczak, 2015). In other words, in either case, the strain rate is much smaller than the commonly used one in previous studies, although it does not preclude a larger strain rate when lithosphere breaks. Finally, considering that faults may have occurred during the Calorian (i.e., one of the five defined time-stratigraphic systems of Mercury, 3.9∼3.5 to 3 Ga b.p.), we choose the strain rate in the range of $4.1\pm1.6\times10^{-20}$ s^{-1} as same as Crane and Klimczak (2017).

The data of the initial temperature profile over depth at the time of 3.8 Ga b.p. is saved in a formatted text file, which can be accessed on Zenodo through the link we provide, and part of the major basic parameters are listed in Table 1.

3.2 Rheology

Regarding the rheology of Mercury's lithosphere. Given the fact that no evidence of plate motion has been found on the surface, it is common to apply power laws (e.g., the dislocation creep) to characterize the rheology of Mercury's outer silicate shell in previous parametric/numerical simulations (e.g., Egea-González et al., 2012; Thiriet et al., 2019). Using this type of rheological law facilitates the planet's silicate shell becoming strong in a short period of time, which helps to produce a large viscosity contrast between the planetary surface and interior, resulting in a complete global plate (Stern et al., 2018; Tosi & Padovan, 2021). However, since we focus on what happened 3.8 billion year ago, should other creep laws be taken into account?

Table 1. Basic Parameters

Symbols	Ref./Description	Values	Units
R_p	[1]Planetary radius	2440	km
R	[1]Gas constant	8.3144	$J/(mol \cdot K)$
g	[1]Surface gravitational acceleration	3.7	m/s^2
α	[1]Thermal expansion coefficient	2×10^{-5}	1/K
T_s	[1]Surface temperature	440	K
η_0	[2]Reference viscosity	1×10^{21}	$Pa \cdot s$
$\dot{\epsilon}_b$	[3]Background bulk strain rate	4.1×10^{-20}	1/s
Q^0_{crust}	[4]Initial crustal heating rate	9.37×10^{-11}	W/kg
Q^0_{mantle}	[4]Initial mantle heating rate	9.37×10^{-12}	W/kg
T_{ref}	[4]Reference temperature	750	K

Ref.:1.Knibbe and van Westrenen (2018); 2.Thiriet et al. (2019)
Ref.:3.Crane and Klimczak (2019); 4.:Xie et al. (2022)

Laboratory studies show that temperature, pressure and strain rate are the main factors controlling the rheology of rocky planets (e.g., Karato & Wu, 1993; Mei et al., 2010; Burov, 2011). Experiments suggest that for lower temperatures (approximately lower than 800 K) and high strain rate, restrictions to glide of dislocations limits rates of straining, the deformation processes abide by Peierls creep, while for higher temperatures region, diffusion creep and power-law play the key role due to their strong sensitivity of temperature and strain rate (e.g., Kameyama et al., 1999; Mei et al., 2010; Molnar, 2020; Pleus et al., 2020). Prior numerical studies targeting at the formation of shear zone suggested that the mechanical discontinuity tends to induce strain localization under lithospheric conditions, resulting in the formation of local region with high effective strain rate (e.g., Schmalholz & Duretz, 2015; Auzemery et al., 2020), which is indicative of the research on the thrust fault-related landforms on Mercury. Combing with the initial temperature profile (i.e., 440 K to 1435 K), the involvement of creep laws like Peierls creep in both the crust and part of the lithosphere-mantle seems to be reasonable. In the end, we apply a composite rheological model that incorporates the rheological laws of Peierls, diffusion and dislocation, assuming that the viscosity is expressed as the pseudo-harmonic average of those three rheologies under isotropic applied stress.

The Peierls creep is given by (e.g., McCarthy et al., 2020):

$$\eta_p = \frac{\gamma \sigma p}{2(A(\gamma \sigma_p)^n)^{1/(s+n)}} exp(\frac{H}{RT} \cdot \frac{(1-\gamma^p)^q}{s+n})\dot{\epsilon}_{II}^{\frac{1}{s+n}-1} \tag{7}$$

with

$$s = (\frac{H}{RT})pq(1-\gamma^p)^{q-1}\gamma^p \tag{8}$$

Where γ is the fitting parameters, σ_p is the Peierls stress. A is the pre-factor and n is the stress exponent. p and q are the Peierls glide parameters that depend on the geometry of obstacles that limit the dislocation motion. Theoretical considerations suggest that $0 \leq p \leq 1$ and $1 \leq q \leq 2$ (Chowdhury et al., 2017; Jain et al., 2017). $\dot{\epsilon}$ is the effective strain rate, and $H = E + PV$, where E is the activation energy, V is the activation volume, R is the universal gas constant. P and T are pressure and temperature, respectively.

The generic form of dislocation creep law and diffusion creep law can be expressed as (e.g., Billen & Hirth, 2007):

$$\eta_d = fA^{\frac{-1}{n}} d^{\frac{m_1}{n}} (\dot{\epsilon}^v_{II})^{\frac{1-n}{n}} exp(\frac{E+PV}{nRT}) \tag{9}$$

Where f is a scaling factor that used to decrease the effective viscosity relative to the viscosity resulting from rock deformation experiments. A is the pre-factor, n is the power-law stress component, d is the grain size, m_1 is the grain size exponent, and $\dot{\epsilon}^v_{II}$ is the second invariant of the viscous part of the deviatoric stress tensor. E, P and V have the same definition as mentioned above. For diffusion creep, $n = 1$, $m_1 \neq 0$, while for dislocation creep, $n > 1, m_1 = 0$.

Finally, the viscosity can be expressed as (e.g., O'Neill & Zhang, 2019):

$$\eta = (\sum_i \eta_i^{-1})^{-1} \tag{10}$$

Where i is the index indicating the above three rheological laws.

We also apply the Drcuker-Prager criterion (DP) to limit all the materials that undergo frictional/plastic deformation (Alejano & Bobet, 2015). It has the following form:

$$\tau_{dp} = C_0 \cdot cos(\phi) + P \cdot sin(\phi) \tag{11}$$

Where τ_{dp} is the yield stress of DP in MPa, C_0 is the cohesion, ϕ is the internal friction angle and P is the pressure in MPa.

In case of yielding, the effective viscosity is iteratively reduced until the corresponding stress is equal to the yield stress, resulting in the effective viscosity with the following form (e.g., Schmalholz & Duretz, 2015):

$$\begin{cases} \eta_{eff} = \eta & \tau < \tau_{dp} \\ \eta_{eff} = \frac{\tau_d}{2E_{II}} & \tau > \tau_{dp} \end{cases} \tag{12}$$

Where η_{eff} is the effective viscosity, E_{II} is the square root of the second invariant of the strain rate tensor, with $E_{II} = \sqrt{(\frac{\partial u_1}{\partial x_1})^2 + \frac{1}{4}(\frac{\partial u_1}{\partial x_2} + \frac{\partial u_2}{\partial x_1})^2}$.

3.3 Lithology

In addition to the rheology, lithology is another major factor determining the plastic strength of the lithosphere, because the plastic strength is generally controlled by the weakest constituent that makes up the rock (e.g., Azuma et al., 2014; Katayama, 2021). Recent geochemical works constrained the major surface potential mineralogy of Mercury to plagioclase, pyroxene and olivine. Particularly, in the NSP, it is plagioclase dominated (e.g., Namur & Charlier, 2017; Kaaden et al., 2017). As for the composition of the lithosphere-mantle of Mercury, an olivine-rich mantle is suggested (Namur et al., 2016; Beuthe et al., 2020). Similarly, we assume that a dried olivine enriched lithosphere-mantle is covered by a dried Columbia diabase (mainly composed of plagioclase) enriched crust (Kay & Dombard, 2019; Katayama, 2021), although the precise constituents of Mercury's lithosphere are still poorly constrained.

Lastly, due to the lack of experiments on the diffusion creep of Maryland/Columbia diabase, we use the diffusion creep of plagioclase instead. For the same reason, we apply the same Peierls creep of dry olivine to both the crust and lithosphere-mantle (Mei et al., 2010; Katayama, 2021). The parameters of rheology and lithology (collectively named material model parameters in ASPECT) are given in Table 2 and 3.

3.4 Mechanical structure

Given the initial temperature profile, strain rate and rheological laws, we can calculate the strength profile of the lithosphere through the parameters given in Table 1 to 3. Laboratory studies suggest that there can be three deformation styles of rocks under lithospheric conditions, namely the brittle, semi-brittle and viscous deformation (D. Kohlstedt et al., 1995; Mei et al., 2010). However, the condition under which the transition from brittle to semi-brittle occurs is still poorly understood. Following previous works (e.g., D. Kohlstedt et al., 1995; D. L. Kohlstedt & Mackwell, 2009), we use an empirical rule that the transition is identified once the brittle strength is approximately equal to one-fifth of the plastic strength. Additionally, the Goetze criterion determining the transi-

Table 2. Constant Parameters for Compositional fields

Symbols	Ref./Description	Crust	Lithosphere-mantle	Units
k	[1]Thermal conductivity	1.5	3.5	$\mathrm{W/(m \cdot K)}$
c	[1]Specific heat capacity	1000	1212	$\mathrm{J/(kg \cdot K)}$
ρ	[2]Average density	2950	3200	$\mathrm{kg/m^3}$
C_0	[3]Cohesions	66	66	MPa
μ	[4]Elastic shear modulus	65	140	GPa
ϕ	[*]Internal friction angle	$30, 28$	$28, 30$	degree

Ref.:1.Knibbe and van Westrenen (2018); 2.Beuthe et al. (2020)
Ref.:3.Klimczak (2015); 4.Kay and Dombard (2019)
Ref.:*.Partially refer to Klimczak (2015)

Table 3. Variable Parameters for Compositional fields

Symbols	Description	Crust	Lithosphere-mantle	Units
	[1]Dislocation creep			
E	Activation energy	485	535	kJ/mol
V	Activation volume	-	-	$\mathrm{m^3/mol}$
A	Pre-factor	1.2×10^{-26}	4.85×10^{-17}	$\mathrm{1/(Pa^n \cdot s)}$
n	Stress exponent	4.7	3.5	-
f	Scaling factor	1/2	1/2	-
	[2]Diffusion creep			
E	Activation energy	467	375	kJ/mol
V	Activation volume	-	8.2×10^{-6}	$\mathrm{m^3/mol}$
A	Pre-factor	1.0×10^{-12}	1.5×10^{-15}	$\mathrm{m^{m_1}(Pa \cdot s^{-1})}$
d	Grain size	2.0×10^{-3}	2.0×10^{-3}	m
m_1	Grain size exponent	3	3	-
n	Stress exponent	1	1	-
f	Scaling factor	1/2	1/2	-
	[3]Peierls creep			
H	Activation energy	320	320	kJ/mol
A	Pre-factor	1.4×10^{-9}	1.4×10^{-9}	$\mathrm{1/(Pa^n \cdot s)}$
δ_p	Peierls stress	5.9×10^{9}	5.9×10^{9}	Pa
n	Stress exponent	2	2	-
p	Glide parameter p	0.5	0.5	-
q	Glide parameter q	1	1	-
γ	Scaling factor	0.17	0.17	-

Ref.:1.[Crameri and Kaus (2010); Katayama (2021)]
Ref.:2.[Crameri and Kaus (2010); Schulz et al. (2019)]
Ref.:3.[Mei et al. (2010)]

tion from semi-brittle to viscous deformation is applied (e.g., D. L. Kohlstedt & Mackwell, 2009; Mei et al., 2010; Zhong & Watts, 2013; Bellas et al., 2020), given by (Goetze & Evans, 1979):

$$\tau_g = \frac{1}{2}(\rho g z - P_p) \tag{13}$$

Where τ_g is the shear stress of Goetze criterion in MPa, ρ is the density, g is the surface gravitational acceleration and z is the depth. P_p is the pore pressure, which is ignored in this work.

Finally, the results calculated from Eq.(11-13) and the empirical rule mentioned above will be used to divide the mechanical structure of the lithosphere (see below). However, one can easily notice that the pressure term in Eq.(11) is the total pressure rather than the lithospheric pressure P_l (i.e., under compression condition: $P_l = \rho g z$), raising the question of how to compute the Eq.(11) without knowing the total pressure when model initializing. In recent years, multiple works have been devoted to revealing the relationship between the total and lithospheric pressure (e.g., Gerya, 2015; Marques et al., 2018; Zuza et al., 2020). A rough estimate is that when the internal friction angle (i.e., ϕ) is around 30°, which is commonly applied to studies on Mercury's lithosphere (e.g., Klimczak, 2015), the total pressure can be equivalent to twice the lithospheric pressure under lithospheric conditions (e.g., Zuza et al., 2020). Therefore, the Eq.(11) can be recast as:

$$\tau_{dp} \approx C_0 \cdot cos(\phi) + 2\rho g z \cdot sin(\phi) \tag{14}$$

In order to evaluate the result calculated by Eq.(14), we additionally introduce the Byerlee intermediate-high pressure law (hereinafter referred to as Byerlee law), with the following form (Klimczak, 2015):

$$\begin{cases} \tau_b = 2\rho g z & \rho g z < 110\text{MPa} \\ \tau_b = \frac{1}{2}(2.1\rho g z + 210) & \rho g z > 110\text{MPa} \end{cases} \tag{15}$$

Where τ_b is the shear stress of Byerlee law in MPa, the rest of parameters are the same as in Eq.(13).

The results computed by Eq.(14-15) are shown in Fig 1, and it can found that the deviation between them is not too significant to accept. Given that the total pressure may be more than twice the lithospheric pressure in most scenarios, it would make the deviation smaller (e.g., Gerya, 2015). Therefore, the application of Eq.(14) is reasonable. Nevertheless, it should be noted that the use of Eq.(14) is only valid when model initializing, while we still apply Eq.(11) to subsequent numerical simulation.

Fig 1 illustrates the strength profile of the crust and lithosphere-mantle at the strain rate of 4.1×10^{-20} s^{-1}, via $\tau = 2\eta\dot{\epsilon}$, where $\dot{\epsilon}$ is the effective strain rate, η is the viscosity. Fig 1.A depicts the strength profile of the crust, where CD20 represents the shear strength of Columbia diabase. Correspondingly, CD20/5 represents the one-fifth of the value of CD20.

It can be figured out that,

1. the brittle strength calculated from the Drucker-Prager criterion (red line) intersects with the profile of CD20/5 (purple line) at point A (the corresponding depth is about 8.5 km), indicating that the deformation type in segment OA is brittle, while the deformation type changes to semi-brittle from point A.
2. the Goetze criterion (dashed black line) and the profile of CD20 (orange line) have no intersection, suggesting that there is no transition from semi-brittle to viscous deformation in the crust.

Accordingly, the crust can be divided into the upper crust that undergoes brittle deformation (segment OA) and the semi-brittle region (segment AB). Similarly, Fig1.B shows the strength profile of the lithosphere-mantle. OL20 (orange line) represents the shear strength of Olivine, and OL20/5 (purple line) is one-fifth of that. It is obviously to find out that OL20/5 is always smaller than DP in the lithosphere-mantle (green line), while

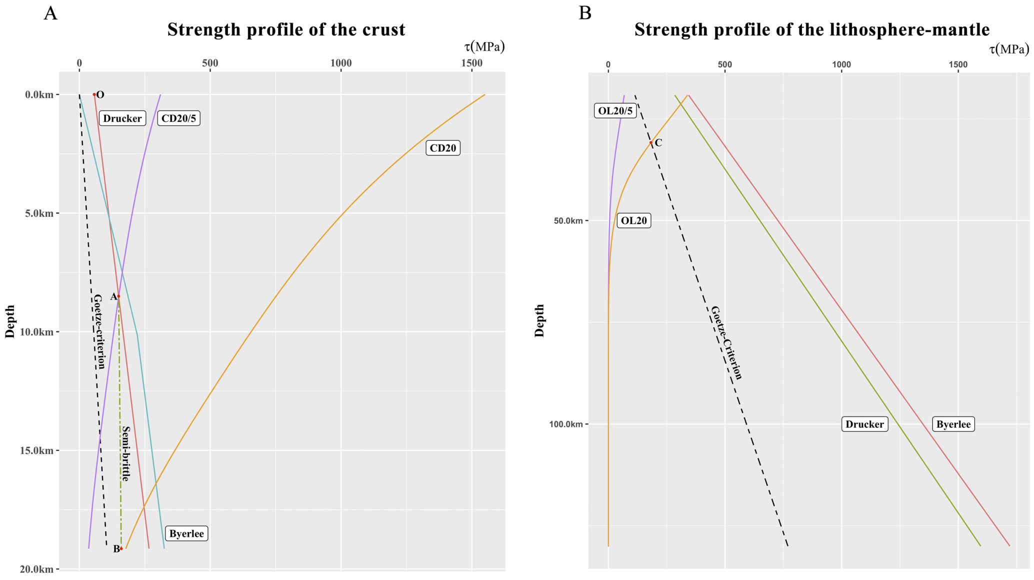

Figure 1. The strength profile of the crust and lithosphere-mantle at the strain rate of 4.1×10^{-20} s^{-1}. In both subplots, the label Drucker and Byerlee respectively indicates the strength profile calculated from Drucker-Prager criterion and Byerlee law. A) In the crust, CD represents the strength profile of Columbia diabase, and CD/5 is one-fifth of that. B) In the lithosphere-mantle, OL represents the strength profile of olivine, and OL/5 is one-fifth of that.

OL20 and Goetze criterion (dashed black line) intersects at point C (the corresponding depth is about 30.85 km). Hence, we can treat the lithosphere-mantle as being made of the semi-brittle region and the rest part (named mantle in this paper).

As a result, the research domain, which initially consisted of the homogenous crust and lithosphere-mantle, is subdivided into four mechanical discontinuous layers (Fig 2). From shallow to deep, they are: the upper crust (z: 0-8.5 km), the semi-brittle region of the crust (z: 8.5-19.1 km), the semi-brittle region of the lithosphere-mantle (z: 19.1-30.85 km) and mantle (z: 30.85-130 km). For those layers with semi-brittle deformation, we can distinguish them by specifying a smaller internal friction coefficient (i.e., a smaller internal friction angle) from other layers when performing numerical simulations (Pleus et al., 2020).

3.5 Geometry configuration

Regarding the model configuration, a cartesian geometry with dimensions of $800\times$ 130 km is applied, where 130 km is the sum of the thickness of the crust and lithosphere-mantle. The mesh of our geometry has a resolution of 125×125 m above the depth of 60 km and 250×250 m below. A topography at the CrMB of 1.5 km (indicator: point U, see Fig 2) is set to account for the lateral heterogenous (Beuthe et al., 2020), which also breaks the symmetry of the model and helps to initialize the convection. This model is heated from the bottom and cooled from the top, while the left and right boundaries are insulated. The top and bottom boundary are free surface and free slip, respectively. A constant strain rate of 4.1×10^{-20} s^{-1} is generated by the horizontal velocity applied on the two lateral boundaries. Fig 2 gives the disproportionate schematic diagram of the geometry model.

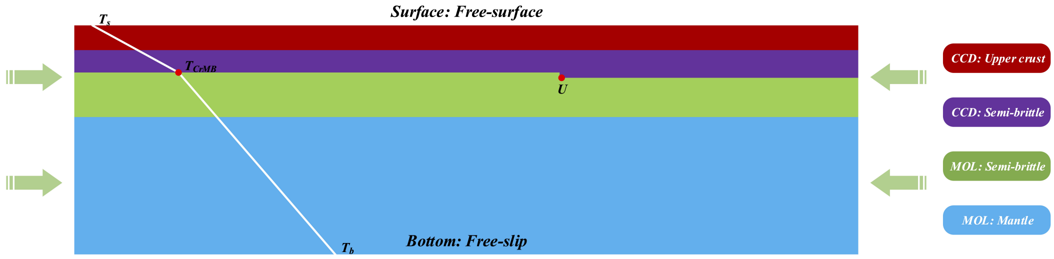

Figure 2. The disproportionate schematic diagram of the geometry model with dimensions of 800×130 km, where the surface temperature (T_s) is 440 K, the temperature at the crust-mantle boundary (T_{CrMB}) is 754 K and the bottom temperature (T_b) is 1435 K. The geometry is composed of a dried Columbia diabase enriched crust and olivine enriched lithosphere-mantle, where the geometry is vertically subdivided into four layers: the upper crust (z: 0-8.5 km) and the crustal semi-brittle region (z: 8.5-19.1 km), lithosphere-mantle semi-brittle region (z: 19.1-30.85 km) and mantle (z: 30.85-130 km). We set up topography (point U as an indicator, its corresponding x-coordinate is 480 km) at the crust-mantle boundary of 1.5 km. This model is heated from the bottom and cooled from the top, while the left and right boundaries are insulated. The top and the bottom boundary are free surface and free slip, respectively. A constant background bulk strain rate of 4.1×10^{-20} s^{-1} is generated by the horizontal velocity applied on the two lateral boundaries. CCD: crustal Columbia diabase. MOL: mantle olivine.

4 Results

Our 2-D numerical simulation starts at 3.8 Ga b.p and lasts for 70 Myr. Fig 3 shows a set of representative results of the square root of the second invariant of the shear strain rate tensor (hereinafter referred to as SRI), which is regarded as the effective strain rate (e.g., Gerya, 2019), at 10 Myr, 40 Myr and 70 Myr with the topography at CrMB of 1.5 km (see Fig 2).

In general, the SRI exhibits a clear spatial distribution pattern. According to the distance from the topography indicator at CrMB (i.e., point U), we divide the high-SRI regions into three sections, namely the section H, section T (framed by black line) and section F. Among them, neither the value nor the concentration of the SRI in the section H has changed much over time, which provides a stable and highly concentrated high-SRI region with an average depth of 10 km, corresponding to the semi-brittle deformation region within the crust. Similarly, we can observe high-SRI region in the section F, but the overall intensity is lower in comparison to section H, and most notably, it is the most sensitive to time. One can notice that the SRI decreases rapidly along with time, and the relative high-SRI region gradually moves into the lithosphere-mantle, corresponding to the semi-brittle region in the lithosphere-mantle. The strain status in section T is the most complicated, where the strain localization occurs due to the proximity to the topography at the CrMB. Although we can find out that the localization seems to extend throughout the crust (i.e., shear zone), both the magnitude and intensity are smaller than those of works concerning with the formation of shear zones on Earth (e.g., Thielmann & Kaus, 2012; Schmalholz & Duretz, 2015), for which we attribute to the much lower strain rate we applied (refer to section 3.1). In addition, the high-SRI region is progressively concentrated near the surface over time in section T, suggesting that the surface is prone to break. It therefore seems to indicate that these shortening features can be formed in the early stage of the simulation.

Furthermore, we calculate the corresponding surface topography and draw the cross section of the surface topography in Fig 4. In Fig 4, we mark some characteristic points, among which the black point U is used to indicate the relative position of the topogra-

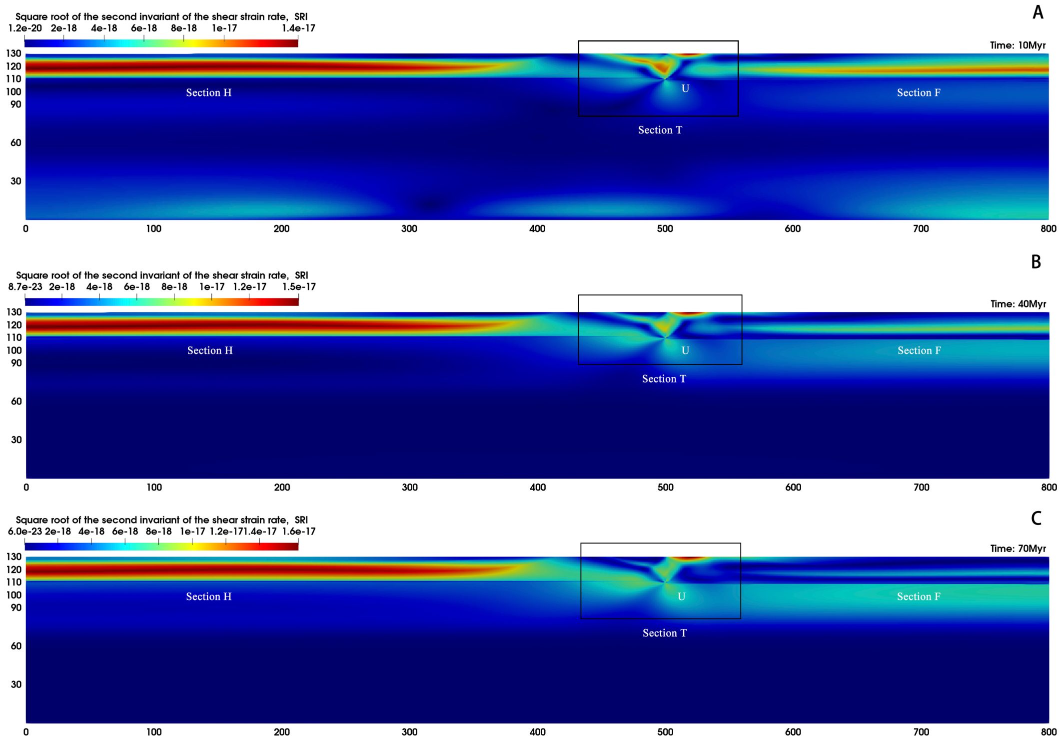

Figure 3. The snapshots of the square root of the second invariant of the shear strain rate (SRI) at A) 10 Myr, B) 40 Myr and C) 70 Myr. The vertical axis represents the y-extension in km, the horizontal axis represents the x-direction extension in km. The high SRI concentrated regions are divided into three sections, from left to right, which are section H, section T (framed by black line) and section F.

phy at the CrMB. The precise values of these markers are listed in Table 4. Geomorphologically, our simulation results in a commonly observed characteristic surface topography on Mercury. Referring to previous geological works (e.g., Byrne et al., 2018; Crane & Klimczak, 2019; Peterson et al., 2020), we also respectively define the segment LS_1A and AS_2B in Fig 4 as the forelimb and the backlimb, in which we can figure out a steep forelimb and a gently sloping backlimb. For comparison, we reference to the morphological profiles of a stack of shortening features in the NSP plotted in Fig2.b from Peterson et al. (2020) and insert it into the Fig 4, the result clearly shows that a well consistent surface topography with the characteristic geomorphic cross section of lobate scarps is obtained (e.g., Watters et al., 2009; Byrne et al., 2018; Klimczak et al., 2019).

According to the data listed in Table 4, the surface topography gradually relaxes but the rate of relaxation is decreasing over the simulation time. we owe the cause of this phenomenon to the change in the strain state within the lithosphere with time. An obvious example is the fading away of the crustal high-SRI regions in section T and F, making the backlimb more gentle along over time. Although the relaxation of the topography is observed, the basic geomorphic features of the surface relief remain stable. The main reason is that, theoretically, we apply the Drucker-Prager criterion to limit all the materials that undergo plastic deformation, in case of yielding, the effective viscosity is iteratively reduced until the corresponding stress is equal to the yield stress. Thus, after the break occurs, the imposed background effective compressive stress is equal to the yield stress, so that makes the surface relief stable in absence of other geological activities like erosion. In addition, for cold rocky planet like Mercury, the gradually increased

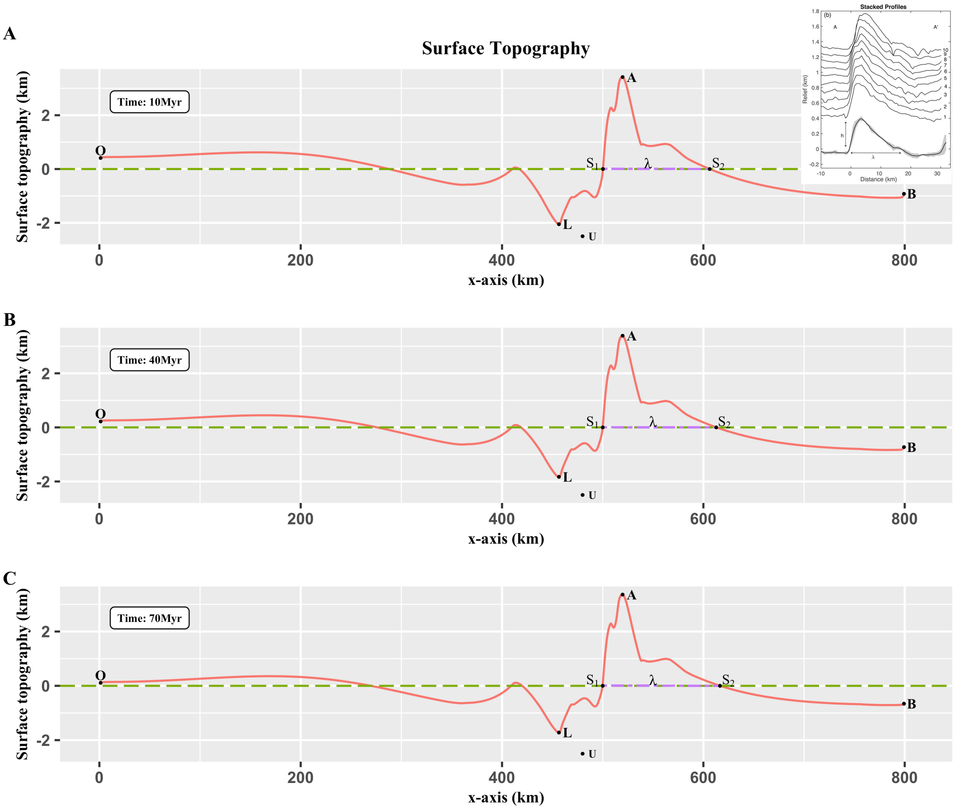

Figure 4. The cross section of the corresponding surface topography (red line) at A) 10 Myr, B) 40 Myr and C) 70 Myr with the topography at CrMB of 1.5 km. The black point U is used to indicate the relative position of the topography at the CrMB. The insertion shows the stacked profiles of several shortening features in the northern smooth plains, which is referenced to the Fig2.b in Peterson et al. (2020).

effective viscosity of Mercury's interior also ensures the maintenance of the surface relief (Hemingway & Matsuyama, 2017).

5 Discussion

For numerical simulation, it is sensitive to the input parameters. In this regard, we spend a lot of contents on selection and calculation of the parameters that may have great impact in section 3. Given that our goal of this paper is to propose a new mechanical model allowing for a mechanically discontinuous lithosphere as well as to obtain a geomorphic consistent surface topography with thrust fault-related landforms in the NSP, and the fact that the information like burial depth or thickness of the weak layer is poorly constrained. As a result, this paper achieves this goal, we therefore do not give more discussions to account for the parameters' uncertainties. Nevertheless, we are still aware of the potential influence of the topography at crust-mantle boundary on the surface relief, as it may be related to which mechanism the surface topography is compensated by (e.g., Watts, 2001). However, a detailed investigation into the compensation state of the crust is obviously beyond the scope of this paper, we hence simply compare the results by adjusting the topography at the CrMB to explore the relationship between surface relief and the interface topography, in which the topography at the CrMB ranges from

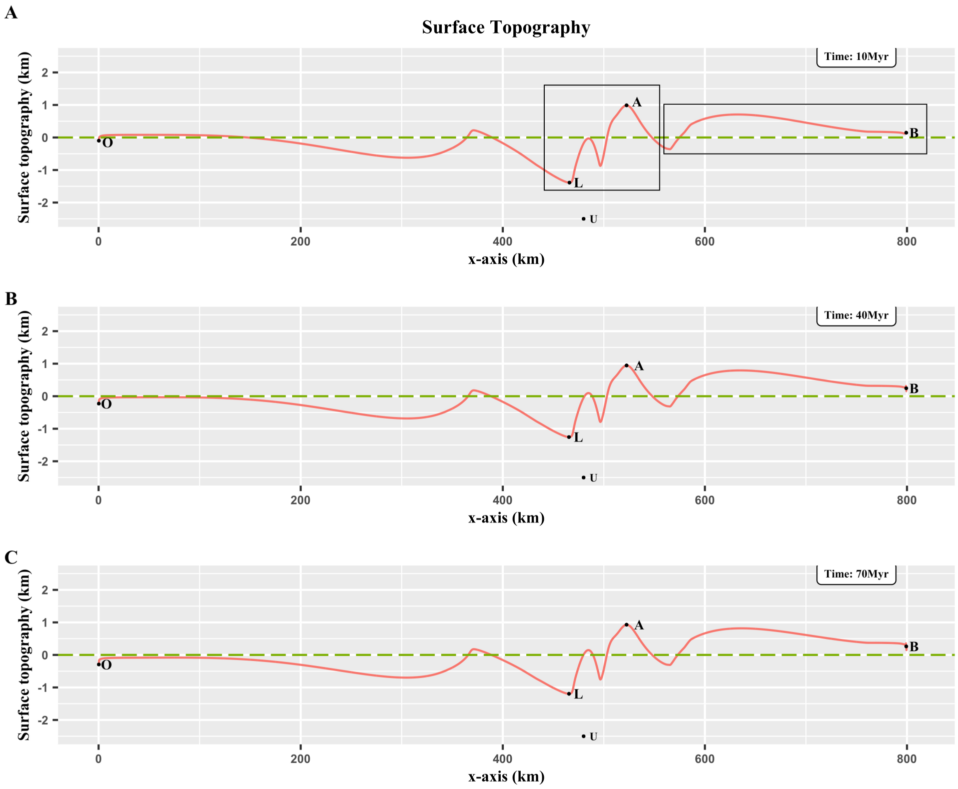

Figure 5. The cross section of the surface topography (red line) at A) 10 Myr, B) 40 Myr and C) 70 Myr with the topography at CrMB of 1 km. The black point U is used to indicate the relative position of the topography at the CrMB.

0.5 to 1.5 km. We present the result with the topography of 1 km in Fig 5, while the rest of the results are shown in supporting information (FigS1 to FigS3). Overall, with the increase of the topography at the CrMB, the surface relief is closer to what is shown in Fig 4. For the areas of interest, such as the areas framed by the black frame in Fig 5, it can be seen that the surface relief is gentler and it shows more tectonic patterns of shortening features compared to that of Fig 4. We owe the main reason to that a larger topography is more likely to induce dramatic strain localization as well as the formation for higher surface relief. According to the detailed tectonic maps drawn by several prior works, the dominated thrust fault-related landforms in the NSP show complex patterns in terms of relief, orientation and extension (e.g., Crane & Klimczak, 2019). Our results suggest that the surface relief may be closely related to the topography at the CrMB, which also stresses that high resolution gravity and topography maps are urgently needed, as they can be used to recur the subsurface architecture (Wieczorek & Phillips, 1997). Another interesting phenomena is that these features appear to be formed in a short period of time on geological time scales (i.e., 10 million years). Stratigraphic studies show that the formation of most of Mercury's shortening landforms are concentrated in specific geological period, and the compressive stress driving the shortening tectonic activities decreases along with time (e.g., Giacomini et al., 2015; Crane & Klimczak, 2017). Collectively, our simulation is able to capture the key features of the process of the formation for thrust fault-related landforms.

So far, the driven forces that make the current landforms have not been fully identified. If the compressive stress were derived solely from Mercury's contraction, the faults

Table 4. The precise values of surface topographical indicators over time

Symbols	10 Myr	40 Myr	70 Myr	Units
O	0.7137	0.2297	0.1146	km
L	-2.0503	-1.8365	-1.7212	km
A	3.4208	3.3902	3.3654	km
B	-0.9239	-0.7346	-0.6679	km
λ	106	112.75	116.6	km

should be uniformly distributed across the planet, which is contradictory to observations (e.g., Watters et al., 2009, 2015). Candidate participants including the tidal force (Klimczak et al., 2015), insolation (Williams et al., 2011) and mantle downwelling (Watters et al., 2021) have been suggested to have contribution to the distribution of the observed features. As the name suggested, the most significant feature of the smooth plains is the volcanically resurfaced surface, with large-volume volcanism being suggested to had ceased around 3.5 billion years ago, younger than the most observed shortening features in smooth plains (e.g., Byrne et al., 2016; Thomas & Rothery, 2019). Surface thick volcanic deposits are thought to have contributions to the formation for thrust faults in the NSP (e.g., Peterson et al., 2019, 2020). Moreover, there are studies suggesting that the volcanic activities play a role especially in regionally or locally tectonic actives (Crane & Klimczak, 2019; Peterson et al., 2020), one evidence is the increased frequency of thrust fault-related landforms within volcanically filled basins suggested by Watters et al. (2009). Therefore, the influence of the long-standing volcanism as well as other tectonic activities and outer-source events like impact on the formation (e.g., Marchi et al., 2013), distribution and orientation of thrust fault-related landforms in the NSP remains to be revealed. Likewise, the contribution from the topography at the crust-mantle boundary deserves further investigation.

Lastly, for the weak layer itself. As mentioned earlier, neither the thickness nor the constituent of this structure is well constrained. But it is most likely made up of an impact product named megaregolith that was buried by subsequence volcanic activities (e.g., Byrne et al., 2014; Watters et al., 2015). As being defined as a highly fragmented structure with low thermal conductivity, megaregolith shows excellent insulation performance (Xie et al., 2022). Therefore, in addition to the fragility of the weak layer, its influence on the thermal dynamic process should also be concerned. For example, the retention of interior heat could facilitate a low degree of contraction (Watters, 2021) or prolongation of volcanism (Byrne et al., 2016).

6 Conclusion

In this paper, we propose a new mechanical model allowing for a mechanically discontinuous lithosphere beneath the northern smooth plains of Mercury. This work is tested with open-source finite-element mantle convection code, resulting in high strain rate region equivalent to weak layer at shallow depth and geomorphic consistent surface topography with typical thrust fault-related landforms. Geomorphically steady surface relief suggests that these shortening features were formed in a short period of time on geological time scales. Mechanically, our model divides the lithosphere into several discontinuous layers by introducing the deformation style of semi-brittle, filling the blank between the brittle and viscous deformation zone (e.g., Zuber et al., 2010; Egea-González et al., 2012). Although the properties and dynamics of semi-brittle deformation are still poorly constrained, the application of such deformation zone to planetary science is still promising, especially thin-rooted tectonic landforms are also reported on other terrestrial planets (e.g., Andrews-Hanna, 2020). We are also aware of the potential influence of the interface at the crust-mantle boundary and volcanism on the formation, distribution, re-

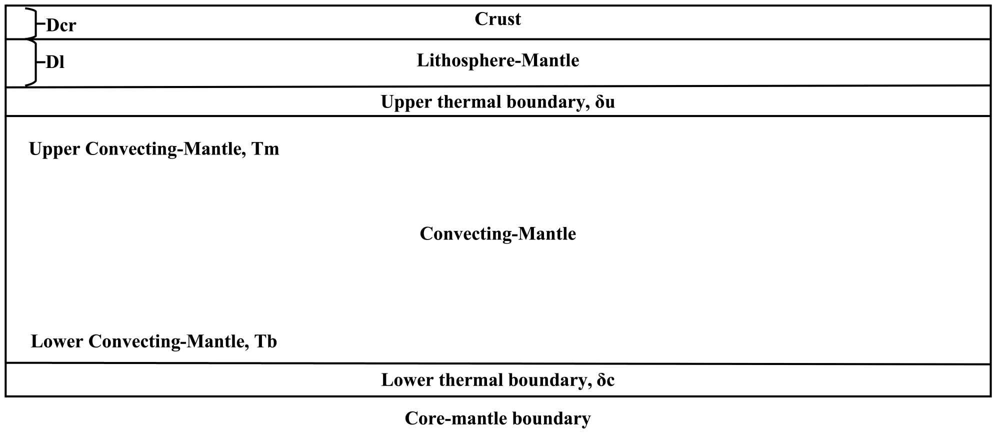

Figure A1. The disproportionate schematic diagram of the 1-D global parametric model of Mercury. This model radially divides the planet into several layers: the crust, lithosphere-mantle, upper/lower thermal boundary, convecting mantle and the outer/inner core (not displayed).

lief and orientation of the shortening features. Additional set of numerical simulations reveals that larger topography at the crust-mantle boundary facilitates the formation for higher surface relief, which also emphasizes that high resolution of gravity and topography maps are urgently needed, as they can be used to recur the subsurface architecture. Because of that, we are looking forward to the upcoming BepiColombo era (Benkhoff et al., 2010).

Acknowledgments
This work is supported by National Natural Science Foundation of China under award 11973072 and 12173068. The computational resources utilized in this research were provided by Shanghai Supercomputer Center. We also thank the Computational Infrastructure for Geodynamics (geodynamics.org) which is funded by the National Science Foundation under award EAR-0949446 and EAR-1550901 for supporting the development of ASPECT.

7 Open Research

The codes that reproduce the outputs of the 2-D numerical simulations are available on Zenodo (`https://doi.org/10.5281/zenodo.6420076`).

Appendix A The 1-D parametric model

The 1-D parametric global evolution model Mercury radially divides the planet into several layers (refer to Fig A1), where the evolutionary process over time of each layer is controlled by its own energy-related equation. By inputting initial parameters, these equations can be literately solved until stable, self-consistent results are obtained. In this appendix, we list the set of major equations describing the energy exchange in Mercury's silicate shell. Detailed description of this model can be found in Xie et al. (2022).

The heat transfer in the crust is controlled by the 1-D steady conduction equation with radiogenic heat production, which is given by:

$$\frac{d}{dr}(r^2 k_{cr} \frac{dT}{dr}) = -r^2 H_{cr} \tag{A1}$$

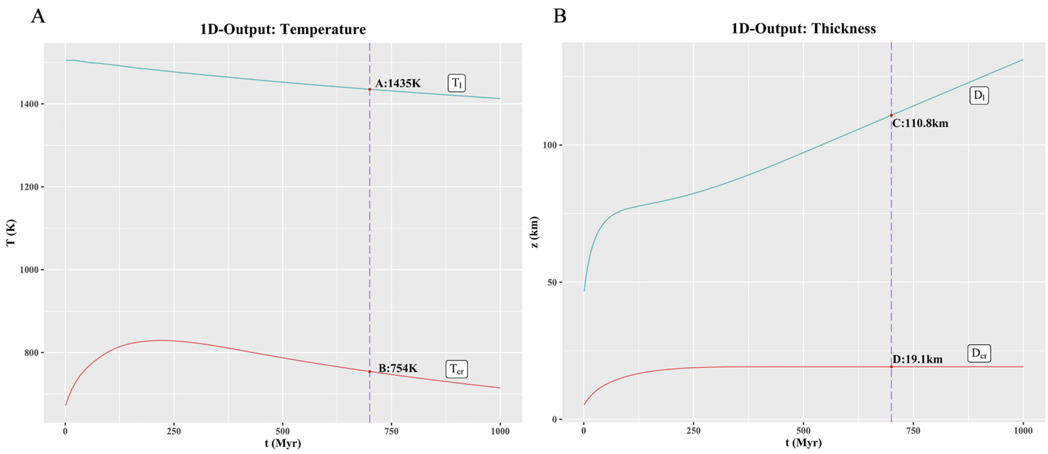

Figure A2. Output of the 1-D global parametric model of Mercury for the first billion years. The vertical dashed purple line indicates the time at 700 million years (i.e., 3.8 Ga b.p), and its four intersections with other curves (i.e., A, B, C and D) respectively represent: A. The temperature at the bottom of the lithosphere-mantle (T_l), B. crust (T_{cr}). C. The thickness of the lithosphere-mantle (D_l), D. crust (D_{cr}).

Where r is radius, k_{cr} is the thermal conductivity of the crust, H_{cr} is the radiogenic heating source in the crust.

For the lithosphere-mantle, its thickness variation depends on the energy equation at the base of the lithosphere-mantle, it can be expressed as (e.g., Morschhauser et al., 2011):

$$\rho_m c_m (T_m - T_l)\frac{dD_l}{dt} + k_m \frac{T_l - T_m}{\delta_u} + k_m \frac{T_c - T_b}{\delta_c} = (\rho_{cr} L_{cr} + \rho_{cr} c_{cr}(T_m - T_l))\frac{dD_{cr}}{dt} \quad \text{(A2)}$$

Where ρ_m and c_m are the average density and specific heat capacity of the mantle, respectively. T_m is the temperature at the upper convecting mantle and T_l is the temperature at the base of the lithosphere-mantle. k_m is the mantle's thermal conductivity, T_c is the temperature at the core-mantle boundary and T_b is the temperature at the lower convecting mantle. δ_u and δ_c respectively represent the thickness of the upper and lower thermal boundary. ρ_{cr} is the average density of the crust, L_{cr} is the latent heat of fusion and c_{cr} is the specific heat capacity of the crust.

The energy equation of the convecting mantle is (e.g., Morschhauser et al., 2011):

$$\epsilon_m V_{cm} \rho_m c_m (1+st)\frac{dT_m}{dt} + (\rho_{cr} L_{cr} + \rho_{cr} c_{cr}(T_m - T_l)\frac{dD_{cr}}{dt})A_{cm} = k_m \frac{T_c - T_b}{\delta_c} + V_{cm} Q_m \quad \text{(A3)}$$

Where ϵ_m is the ratio of the convecting mantle's temperature to the average temperature of the convecting mantle, V_{cm} and A_{cm} are the volume and the surface area of this layer. Q_m is the radiogenic heat production rate in the convecting mantle. st is the stefan number that accounts for the consumption and release of latent heat during crystallization and melting of mantle rock.

The results for the first 1 billion years are shown in Fig A2, including the temperature at the bottom of the crust (T_{cr}) and lithosphere-mantle (T_l) over time, the thickness of the crust (D_{cr}) and lithosphere-mantle (D_l) over time. In both subfigures, the purple vertical dashed line indicates the time at 7 million years, i.e., 3.8 Ga b.p.

References

Alejano, L. R., & Bobet, A. (2015). Drucker–prager criterion. In R. Ulusay (Ed.), *The isrm suggested methods for rock characterization, testing and monitoring: 2007-2014* (pp. 247–252). Cham: Springer International Publishing. Retrieved from https://doi.org/10.1007/978-3-319-07713-0_22 doi: 10.1007/978-3-319-07713-0_22

Andrews-Hanna, J. C. (2020). The tectonic architecture of wrinkle ridges on mars. *Icarus*, *351*, 113937. Retrieved from https://www.sciencedirect.com/science/article/pii/S0019103520303110 doi: https://doi.org/10.1016/j.icarus.2020.113937

Auzemery, A., Willingshofer, E., Yamato, P., Duretz, T., & Sokoutis, D. (2020). Strain localization mechanisms for subduction initiation at passive margins. *Global and Planetary Change*, *195*, 103323.

Azuma, S., Katayama, I., & Nakakuki, T. (2014). Rheological decoupling at the moho and implication to venusian tectonics. *Scientific Reports*, *4*.

Banks, M. E., Xiao, Z., Watters, T. R., Strom, R. G., Braden, S. E., Chapman, C. R., ... Byrne, P. K. (2015). Duration of activity on lobate-scarp thrust faults on mercury. *Journal of Geophysical Research: Planets*, *120*(11), 1751–1762.

Bellas, A., Zhong, S., & Watts, A. (2020). Constraints on the rheology of the lithosphere from flexure of the pacific plate at the hawaiian islands. *Geochemistry, Geophysics, Geosystems*, *21*(2), e2019GC008819.

Benkhoff, J., van Casteren, J., Hayakawa, H., Fujimoto, M., Laakso, H., Novara, M., ... Ziethe, R. (2010). Bepicolombo—comprehensive exploration of mercury: Mission overview and science goals. *Planetary and Space Science*, *58*(1), 2-20. Retrieved from https://www.sciencedirect.com/science/article/pii/S0032063309002840 (Comprehensive Science Investigations of Mercury: The scientific goals of the joint ESA/JAXA mission BepiColombo) doi: https://doi.org/10.1016/j.pss.2009.09.020

Beuthe, M., Charlier, B., Namur, O., Rivoldini, A., & Van Hoolst, T. (2020). Mercury's crustal thickness correlates with lateral variations in mantle melt production. *Geophysical Research Letters*, *47*(9), e2020GL087261.

Billen, M. I., & Hirth, G. (2007). Rheologic controls on slab dynamics. *Geochemistry, Geophysics, Geosystems*, *8*(8).

Burov, E. B. (2011). Rheology and strength of the lithosphere. *Marine and Petroleum Geology*, *28*(8), 1402–1443.

Byrne, P. K., Klimczak, C., & Şengör, A. (2018). The tectonic character of mercury. *Mercury. The View after MESSENGER. Edited by Sean C. Solomon*, 249–286.

Byrne, P. K., Klimczak, C., Şengör, A. C., Solomon, S. C., Watters, T. R., Hauck, S. A., et al. (2014). Mercury's global contraction much greater than earlier estimates. *Nature Geoscience*, *7*(4), 301–307.

Byrne, P. K., Ostrach, L. R., Fassett, C. I., Chapman, C. R., Denevi, B. W., Evans, A. J., ... Solomon, S. C. (2016). Widespread effusive volcanism on mercury likely ended by about 3.5 ga. *Geophysical Research Letters*, *43*(14), 7408–7416.

Chowdhury, P., Gerya, T., & Chakraborty, S. (2017). Emergence of silicic continents as the lower crust peels off on a hot plate-tectonic earth. *Nature Geoscience*, *10*(9), 698–703.

Crameri, F., & Kaus, B. J. (2010). Parameters that control lithospheric-scale thermal localization on terrestrial planets. *Geophysical Research Letters*, *37*(9).

Crane, K. T., & Klimczak, C. (2017). Timing and rate of global contraction on mercury. *Geophysical Research Letters*, *44*(7), 3082–3089.

Crane, K. T., & Klimczak, C. (2019). Tectonic patterns of shortening landforms in mercury's northern smooth plains. *Icarus*, *317*, 66–80.

Denevi, B. W., Ernst, C. M., Meyer, H. M., Robinson, M. S., Murchie, S. L., Whitten, J. L., ... others (2013). The distribution and origin of smooth plains on mercury. *Journal of Geophysical Research: Planets*, *118*(5), 891–907.

Du, J., Wieczorek, M. A., & Fa, W. (2020). Thickness of lava flows within the northern smooth plains on mercury as estimated by partially buried craters. *Geophysical Research Letters*, *47*(20), e2020GL090578.

Egea-González, I., Ruiz, J., Fernández, C., Williams, J.-P., Márquez, Á., & Lara, L. M. (2012). Depth of faulting and ancient heat flows in the kuiper region of mercury from lobate scarp topography. *Planetary and Space Science*, *60*(1), 193–198.

Gerya, T. (2015). Tectonic overpressure and underpressure in lithospheric tectonics and metamorphism. *Journal of Metamorphic Geology*, *33*(8), 785–800.

Gerya, T. (2019). *Introduction to numerical geodynamic modelling.* Cambridge University Press.

Giacomini, L., Massironi, M., Galluzzi, V., Ferrari, S., & Palumbo, P. (2020). Dating long thrust systems on mercury: New clues on the thermal evolution of the planet. *Geoscience Frontiers*, *11*(3), 855–870.

Giacomini, L., Massironi, M., Marchi, S., Fassett, C., Di Achille, G., & Cremonese, G. (2015). Age dating of an extensive thrust system on mercury: implications for the planet's thermal evolution. *Geological Society, London, Special Publications*, *401*(1), 291–311.

Goetze, C., & Evans, B. (1979). Stress and temperature in the bending lithosphere as constrained by experimental rock mechanics. *Geophysical Journal International*, *59*(3), 463–478.

Head, J. W., Chapman, C. R., Strom, R. G., Fassett, C. I., Denevi, B. W., Blewett, D. T., ... others (2011). Flood volcanism in the northern high latitudes of mercury revealed by messenger. *Science*, *333*(6051), 1853–1856.

Heister, T., Dannberg, J., Gassmöller, R., & Bangerth, W. (2017). High accuracy mantle convection simulation through modern numerical methods–ii: realistic models and problems. *Geophysical Journal International*, *210*(2), 833–851.

Hemingway, D. J., & Matsuyama, I. (2017). Isostatic equilibrium in spherical coordinates and implications for crustal thickness on the moon, mars, enceladus, and elsewhere. *Geophysical Research Letters*, *44*(15), 7695-7705. Retrieved from `https://agupubs.onlinelibrary.wiley.com/doi/abs/10.1002/2017GL073334` doi: https://doi.org/10.1002/2017GL073334

Jain, C., Korenaga, J., & Karato, S.-i. (2017). On the yield strength of oceanic lithosphere. *Geophysical Research Letters*, *44*(19), 9716–9722.

Kaaden, K. E. V., McCubbin, F. M., Nittler, L. R., Peplowski, P. N., Weider, S. Z., Frank, E. A., & Mccoy, T. J. (2017). Geochemistry, mineralogy, and petrology of boninitic and komatiitic rocks on the mercurian surface: Insights into the mercurian mantle. *Icarus*, *285*, 155-168.

Kameyama, M., Yuen, D. A., & Karato, S.-I. (1999). Thermal-mechanical effects of low-temperature plasticity (the peierls mechanism) on the deformation of a viscoelastic shear zone. *Earth and Planetary Science Letters*, *168*(1-2), 159–172.

Karato, S.-i., & Wu, P. (1993). Rheology of the upper mantle: A synthesis. *Science*, *260*(5109), 771–778.

Katayama, I. (2021). Strength models of the terrestrial planets and implications for their lithospheric structure and evolution. *Progress in Earth and Planetary Science*, *8*(1), 1–17.

Kay, J. P., & Dombard, A. J. (2019). Long-wavelength topography on mercury is not from folding of the lithosphere. *Icarus*, *319*, 724–728.

Klimczak, C. (2015). Limits on the brittle strength of planetary lithospheres undergoing global contraction. *Journal of Geophysical Research: Planets*, *120*(12), 2135–2151.

Klimczak, C., Byrne, P. K., Şengör, A. C., & Solomon, S. C. (2019). Principles of structural geology on rocky planets. *Canadian Journal of Earth Sciences*, *56*(12), 1437–1457.

Klimczak, C., Byrne, P. K., & Solomon, S. C. (2015). A rock-mechanical assessment of mercury's global tectonic fabric. *Earth and Planetary Science Letters*, *416*, 82–90.

Knibbe, J. S., & van Westrenen, W. (2018). The thermal evolution of mercury's fe–si core. *Earth and Planetary Science Letters*, *482*, 147–159.

Kohlstedt, D., Evans, B., & Mackwell, S. (1995). Strength of the lithosphere: Constraints imposed by laboratory experiments. *Journal of Geophysical Research: Solid Earth*, *100*(B9), 17587–17602.

Kohlstedt, D. L., & Mackwell, S. J. (2009). Strength and deformation of planetary lithospheres. In T. R. Watters & R. A. Schultz (Eds.), *Planetary tectonics* (p. 397–456). Cambridge University Press. doi: 10.1017/CBO9780511691645.010

Kronbichler, M., Heister, T., & Bangerth, W. (2012). High accuracy mantle convection simulation through modern numerical methods. *Geophysical Journal International*, *191*(1), 12–29.

Marchi, S., Chapman, C. R., Fassett, C. I., Head, J. W., Bottke, W. F., & Strom, R. G. (2013, Jul 01). Global resurfacing of mercury 4.0–4.1 billion years ago by heavy bombardment and volcanism. *Nature*, *499*(7456), 59-61. Retrieved from `https://doi.org/10.1038/nature12280` doi: 10.1038/nature12280

Marques, F., Ranalli, G., & Mandal, N. (2018). Tectonic overpressure at shallow depth in the lithosphere: The effects of boundary conditions. *Tectonophysics*, *746*, 702–715.

McCarthy, A., Tugend, J., Mohn, G., Candioti, L., Chelle-Michou, C., Arculus, R., ... Müntener, O. (2020). A case of ampferer-type subduction and consequences for the alps and the pyrenees. *American Journal of Science*, *320*(4), 313–372.

Mei, S., Suzuki, A., Kohlstedt, D., Dixon, N., & Durham, W. (2010). Experimental constraints on the strength of the lithospheric mantle. *Journal of Geophysical Research: Solid Earth*, *115*(B8).

Michel, N. C., Hauck, S. A., Solomon, S. C., Phillips, R. J., Roberts, J. H., & Zuber, M. T. (2013). Thermal evolution of mercury as constrained by messenger observations. *Journal of Geophysical Research: Planets*, *118*(5), 1033–1044.

Molnar, P. (2020). The brittle-plastic transition, earthquakes, temperatures, and strain rates. *Journal of Geophysical Research: Solid Earth*, *125*(7), e2019JB019335.

Moresi, L., Dufour, F., & Mühlhaus, H.-B. (2003). A lagrangian integration point finite element method for large deformation modeling of viscoelastic geomaterials. *Journal of computational physics*, *184*(2), 476–497.

Morschhauser, A., Grott, M., & Breuer, D. (2011). Crustal recycling, mantle dehydration, and the thermal evolution of mars. *Icarus*, *212*(2), 541-558. Retrieved from `https://www.sciencedirect.com/science/article/pii/S0019103510004963` doi: https://doi.org/10.1016/j.icarus.2010.12.028

Namur, O., & Charlier, B. (2017). Silicate mineralogy at the surface of mercury. *Nature Geoscience*, *10*(1), 9–13.

Namur, O., Collinet, M., Charlier, B., Grove, T. L., Holtz, F., & McCammon, C. (2016). Melting processes and mantle sources of lavas on mercury. *Earth and Planetary Science Letters*, *439*, 117–128.

Nimmo, F., & Watters, T. R. (2004). Depth of faulting on mercury: Implications for heat flux and crustal and effective elastic thickness. *Geophysical Research Letters*, *31*(2). Retrieved from `https://agupubs.onlinelibrary.wiley.com/doi/abs/10.1029/2003GL018847` doi: https://doi.org/10.1029/2003GL018847

O'Neill, C., & Zhang, S. (2019). Chapter 4 - modeling early earth tectonics: The case for stagnant lid behavior. In M. J. Van Kranendonk, V. C. Bennett, & J. E. Hoffmann (Eds.), *Earth's oldest rocks (second edition)* (Second Edition ed., p. 65-80). Elsevier. Retrieved from `https://www.sciencedirect.com/science/article/pii/B9780444639011000046` doi: https://doi.org/10.1016/B978-0-444-63901-1.00004-6

Ostrach, L. R., Robinson, M. S., Whitten, J. L., Fassett, C. I., Strom, R. G., Head, J. W., & Solomon, S. C. (2015). Extent, age, and resurfacing history of the northern smooth plains on mercury from messenger observations. *Icarus*, *250*, 602–622.

Peplowski, P. N., Evans, L. G., Hauck, S. A., McCoy, T. J., Boynton, W. V., Gillis-Davis, J. J., ... others (2011). Radioactive elements on mercury's surface from messenger: Implications for the planet's formation and evolution. *science*, *333*(6051), 1850–1852.

Peterson, G. A., Johnson, C. L., Byrne, P. K., & Phillips, R. J. (2019). Distribution of areal strain on mercury: Insights into the interaction of volcanism and global contraction. *Geophysical Research Letters*, *46*(2), 608-615. Retrieved from `https://agupubs.onlinelibrary.wiley.com/doi/abs/10.1029/2018GL080749` doi: https://doi.org/10.1029/2018GL080749

Peterson, G. A., Johnson, C. L., Byrne, P. K., & Phillips, R. J. (2020). Fault structure and origin of compressional tectonic features within the smooth plains on mercury. *Journal of Geophysical Research: Planets*, *125*(7), e2019JE006183.

Pleus, A., Ito, G., Wessel, P., & Frazer, L. N. (2020). Rheology and thermal structure of the lithosphere beneath the hawaiian ridge inferred from gravity data and models of plate flexure. *Geophysical Journal International*, *222*, 207-224.

Schmalholz, S. M., & Duretz, T. (2015). Shear zone and nappe formation by thermal softening, related stress and temperature evolution, and application to the alps. *Journal of Metamorphic Geology*, *33*, 887-908.

Schmalholz, S. M., Duretz, T., Hetényi, G., & Medvedev, S. (2018). Distribution and magnitude of stress due to lateral variation of gravitational potential energy between indian lowland and tibetan plateau. *Geophysical Journal International*.

Schulz, F. T., Tosi, N., Plesa, A., & Breuer, D. (2019). Stagnant-lid convection with diffusion and dislocation creep rheology: Influence of a non-evolving grain size. *Geophysical Journal International*.

Solomon, S. C., Nittler, L. R., & Anderson, B. J. (2018). *Mercury: The view after messenger* (Vol. 21). Cambridge University Press.

Stern, R. J., Gerya, T. V., & Tackley, P. J. (2018). Stagnant lid tectonics: Perspectives from silicate planets, dwarf planets, large moons, and large asteroids. *Geoscience frontiers*, *9*, 103-119.

Thielmann, M., & Kaus, B. J. P. (2012). Shear heating induced lithospheric-scale localization: Does it result in subduction? *Earth and Planetary Science Letters*, *359*, 1-13.

Thiriet, M., Breuer, D., Michaut, C., & Plesa, A. (2019). Scaling laws of convection for cooling planets in a stagnant lid regime. *Physics of the Earth and Planetary Interiors*.

Thomas, R. J., & Rothery, D. A. (2019, 02). Volcanism on Mercury. *Elements*, *15*(1), 27-32. Retrieved from `https://doi.org/10.2138/gselements.15.1.27` doi: 10.2138/gselements.15.1.27

Tosi, N., & Padovan, S. (2021). Mercury, moon, mars. In *Mantle convection and surface expressions* (p. 455-489). American Geophysical Union (AGU). Retrieved from `https://agupubs.onlinelibrary.wiley.com/doi/abs/10.1002/9781119528609.ch17` doi: https://doi.org/10.1002/9781119528609.ch17

Watters, T. R. (2021). A case for limited global contraction of mercury. *Communications Earth & Environment*, *2*.

Watters, T. R., James, P. B., & Selvans, M. M. (2021). Mercury's crustal thickness and contractional strain. *Geophysical Research Letters*.

Watters, T. R., Schultz, R. A., Robinson, M. S., & Cook, A. C. (2002). The mechanical and thermal structure of mercury's early lithosphere. *Geophysical Research Letters*, *29*, 37-1-37-4.

Watters, T. R., Selvans, M. M., Banks, M. E., Hauck II, S. A., Becker, K. J., & Robinson, M. S. (2015). Distribution of large-scale contractional tectonic landforms on mercury: Implications for the origin of global stresses. *Geophysical Research Letters*, *42*(10), 3755-3763. Retrieved from `https://agupubs.onlinelibrary.wiley.com/doi/abs/10.1002/2015GL063570` doi: https://doi.org/10.1002/2015GL063570

Watters, T. R., Solomon, S. C., Robinson, M. S., Head, J. W., Andre, S. L., Hauck, S. A., & Murchie, S. L. (2009). The tectonics of mercury: The view after messenger's first flyby. *Earth and Planetary Science Letters*, *285*, 283-296.

Watts, A. B. (2001). *Isostasy and flexure of the lithosphere.* Cambridge University Press.

Wieczorek, M. A., & Phillips, R. J. (1997). The structure and compensation of the lunar highland crust. *Journal of Geophysical Research: Planets*, *102*(E5), 10933-10943. Retrieved from `https://agupubs.onlinelibrary.wiley.com/doi/abs/10.1029/97JE00666` doi: https://doi.org/10.1029/97JE00666

Williams, J.-P., Ruiz, J., Rosenburg, M. A., Aharonson, O., & Phillips, R. J. (2011). Insolation driven variations of mercury's lithospheric strength. *Journal of Geophysical Research: Planets*, *116*(E1). Retrieved from `https://agupubs.onlinelibrary.wiley.com/doi/abs/10.1029/2010JE003655` doi: https://doi.org/10.1029/2010JE003655

Xie, J.-C., Zhang, M., & Huang, C.-L. (2022). Influence of megaregolith on the thermal evolution of mercury's silicate shell. *Research in Astronomy and Astrophysics*, *22*(3), 035026. Retrieved from `https://doi.org/10.1088/1674-4527/ac4ca1` doi: 10.1088/1674-4527/ac4ca1

Zhong, S., & Watts, A. B. (2013). Lithospheric deformation induced by loading of the hawaiian islands and its implications for mantle rheology. *Journal of Geophysical Research*, *118*, 6025-6048.

Zuber, M. T., Montési, L. G. J., Farmer, G. T., Hauck, S. A., Ritzer, J. A., Phillips, R. J., . . . Johnson, C. L. (2010). Accommodation of lithospheric shortening on mercury from altimetric profiles of ridges and lobate scarps measured during messenger flybys 1 and 2. *Icarus*, *209*, 247-255.

Zuza, A. V., Levy, D. A., & Mulligan, S. R. (2020). Geologic field evidence for non-lithostatic overpressure recorded in the north american cordillera hinterland, northeast nevada. *Geoscience Frontiers*.